Research Article Vol. 9, No. 11 / 1 November 2019 / Optical Materials Express 4165
Optical Materials EXPRESS

Femtosecond laser polishing of germanium [Invited]

LAUREN L. TAYLOR,[1] JING XU,[2] MICHAEL POMERANTZ,[3] THOMAS R. SMITH,[5] JOHN C. LAMBROPOULOS,[2,3,4] AND JIE QIAO[1,*]

[1]Chester F. Carlson Center for Imaging Science, Rochester Institute of Technology, 54 Lomb Memorial Drive, Rochester, NY 14623, USA
[2]Department of Mechanical Engineering, University of Rochester, Rochester NY 14623, USA
[3]Materials Science Program, University of Rochester, Rochester NY 14623, USA
[4]Laboratory for Laser Energetics, University of Rochester, Rochester NY 14623, USA
[5]Aperture Optical Sciences, Meriden, CT 06450, USA
[*]qiao@cis.rit.edu

Abstract: Freeform optics can reduce the cost, weight, and size of advanced imaging systems, but it is challenging to manufacture the complex rotationally asymmetric surfaces to optical tolerances. To address the need for disruptive, high-precision sub-aperture forming and finishing techniques for freeform optics, we investigate an alternative, non-contact polishing methodology using femtosecond lasers, combining modeling, experiments, and demonstrations. Femtosecond-laser-based polishing of germanium was investigated using an experimentally-validated two-temperature model of laser/germanium interaction to guide the understanding and selection of laser parameters to achieve near-nonthermal ablation for polishing and figuring. For the first time to our knowledge, model-guided femtosecond laser polishing of germanium was successfully demonstrated, achieving precision material removal while maintaining single-digit nanometer optical surface quality. The demonstrated femtosecond-laser-based polishing technique lays the foundation for semiconductor optics polishing/fabrication using femtosecond lasers and opens a viable path for high-precision, complex sub-aperture optical polishing tasks on various materials.

1. Introduction

The next generation of imaging systems for applications like consumer electronics, augmented and virtual reality, and space-based telescopes require advanced optical design strategies to reduce the system footprint and weight while maintaining high optical performance [1,2]. One such strategy is the integration of freeform optics having complex, rotationally asymmetric surface geometries to condense the task of a system of spherical optics into a single element [3]. To glean the full advantage of these novel optical elements, a standardized process chain for deterministic fabrication is required. This need has provoked the investigation of disruptive tools and techniques to manufacture sophisticated freeform surfaces to optical tolerances.

State-of-the-art ultraprecision forming and finishing tools for freeform optics include deterministic micro-grinding, diamond turning, raster milling, magnetorheological finishing, atmospheric pressure plasma processing, and ion-beam figuring. These techniques have advanced sub-aperture material removal strategies and flexible tool positioning capabilities which cater to fabricating rotationally asymmetric parts and small, complex surface features [3–9]. However, the sub-aperture material removal strategies leave behind detrimental mid-spatial frequency tool marks on the millimeter scale, and the complexity of sample-tool alignment leads to surface form errors [10,11]. Contact-based polishing methods also generate significant waste and have long lead times for freeform parts which are disadvantageous for high-volume manufacturing. Therefore, there remains a need for alternative forming, finishing, and post-processing tools for fabricating freeform optics.

#374174 https://doi.org/10.1364/OME.9.004165
Journal © 2019 Received 30 Jul 2019; revised 22 Sep 2019; accepted 22 Sep 2019; published 2 Oct 2019

Optical Materials EXPRESS

Over the last decade, lasers have been readily investigated as a non-contact tool for optical polishing tasks owing to their flexible beam delivery and tunable control of material removal. The predominant polishing strategy utilizes continuous wave and/or micro- and nano-second pulsed lasers to melt and re-flow a layer of the material surface. Continuous-wave CO_2 lasers have been used for in-situ healing of laser damage for high-energy laser beam delivery systems and as a smoothing step in a laser-based fabrication chain for freeform optics [12,13]. Micro- and nano-second pulsed lasers have also been used to polish various metals to nanometer-order roughness [14,15]. However, melt-based polishing requires precise laser-wavelength/material matching to enable sufficient linear energy absorption to achieve melting. The thermal nature of the laser interaction also causes detrimental structure changes including large sub-surface melt and heat-affected zones, high spatial frequency ripples due to melt front solidification, and form errors due to the flow of molten material [14,16,17]. These requirements limit both the versatility and precision of laser micro-polishing, which is currently unsuitable for optic-quality polishing tasks.

We investigate a high-precision non-contact laser-based polishing methodology towards freeform fabrication using femtosecond lasers. In contrast to continuous wave and micro- and nano-second laser systems, femtosecond lasers can be focused to GW-TW/cm^2 intensities and have 10^{-15} second pulse durations. These attributes enable precise, spatially-localized ablation-based material removal with minimal thermal impact on various materials having different optical properties [18]. Their unprecedented material removal capabilities have enabled diverse applications in optics and photonics fabrication, such as writing waveguides in glass [19], welding materials with different coefficients of thermal expansion [20], surface texturing [21,22], and post-processing/form correction for laser polished optics [23]. Picosecond lasers have been used for melt-based polishing of metals achieving surface roughness down to the sub-micron level [24,25]. Numerical and qualitative experimental studies comparing nano-, pico-, and femto-second laser ablation have shown that decreasing the pulse width to the ultrafast regime can improve the processing precision towards smoother surfaces [26,27]. However, to our best knowledge, optic-quality, ablation-based femtosecond laser polishing has not been demonstrated.

For femtosecond laser-based polishing, it is imperative to remove material precisely while controlling the onset of thermal and structural effects detrimental to achieving a smooth surface, e.g., significant melting, oxidation, gas bubble/ripple formation, etc. [28,29]. A set of optimal, material-specific laser parameters for precise material removal (e.g., repetition rate, scan speed, and fluence) must be determined. This is a non-trivial task due to the competing influence of different interaction phenomena such as nonthermal melting, ablation, electron-lattice heat transfer, heat accumulation, and thermal melting/oxidation [18]. It is challenging to experimentally determine a set of optimum parameters to effectively balance these mechanisms, as the laser parameters can be tuned in a near-continuous fashion on many femtosecond laser systems and their impact is material-specific.

In this paper, we demonstrate a methodology, modeling, and experimental results for high-precision polishing of germanium using femtosecond lasers, i.e., selectively removing material while maintaining an optic-quality surface. In Section 2, we describe a strategy to achieve ablation and avoid the onset of undesired thermal effects by controlling the combined impact of laser parameters. A Two-Temperature Model was used to investigate the femtosecond laser/germanium interaction mechanism. Section 3 demonstrates that smooth and controllable laser polishing is achieved using a set of model-determined operational laser parameters. In Section 4, we discuss the potential underlying mechanism for femtosecond laser-based polishing of germanium.

2. Numerical modeling to determine key laser parameters

Owing to their high intensities, ultrafast lasers have the capability to induce nonthermal ablation/structural changes, where material breakdown is achieved while the lattice temperature

Optical Materials EXPRESS

remains below the melting point [18,30]. When an ultrafast laser is operated at a high repetition rate (>200 KHz), material can also be removed via heat-accumulation-induced ablation for which solid-liquid-gas phase change occurs. For laser-based polishing, it is critical to precisely remove material while avoiding significant thermal melting and large heat-affected zones, as these affect the structural integrity and final roughness of the laser-processed surface. Although nonthermal ablation is desirable for high-precision polishing, its attainment is highly dependent on the material and the laser parameters, so sometimes it cannot be achieved. Therefore, it is essential to understand the contributing impact of ablation and temperature rise/melting during laser irradiation and to control them to best approach the desired nonthermal ablation conditions for polishing. Numerical modeling of the femtosecond laser/germanium (Ge) interaction process was conducted to achieve this understanding and to determine the potential laser parameters for removing material with minimal thermal effects. The modeling process provides insight and guidance for targeted experiments, as experimental sensitivity studies with a broad parameter matrix are time-consuming and material-expensive.

A three-dimensional Two-Temperature Model (TTM) was constructed to model scanning-based femtosecond laser processing of Ge, based upon models formulated in [30–32]. The TTM simulates how absorption of laser energy drives the generation of a dense, hot system of free-carrier electrons which then collides with and transfers heat to the material lattice until the systems reach thermal equilibrium [30]. The model was used to investigate the sensitivity of the free-carrier electron density and the lattice temperature to different laser parameters. Simulating the free carrier density allows prediction of material breakdown and simulating the lattice temperature rise can predict the onset of thermal melting during processing.

In the TTM simulations, the laser pulse width and wavelength are 300 fs (full width at half-maximum) and 1030 nm. The initial Ge temperature was set to 300 K and the initial carrier density was set to 10^{13} cm^{-3} to mimic the experimental processing environment and sample properties. The TTM equations and additional simulation/influence parameters are detailed in the Appendix.

2.1. Impact of laser fluence

The TTM was first used to investigate the standalone impact of fluence during femtosecond laser/Ge interaction, as it can independently drive the onset of ablation and heating of the material surface. The pulse-induced free-carrier electron number density, carrier-system temperature, and lattice temperature were simulated to predict the potential onset of ablation and melting at different fluences.

Figure 1 compares the TTM results at the material surface and in the spatial center of the incident Gaussian pulse for two different peak fluences: (a) 0.37 J/cm^2 and (b) 0.22 J/cm^2. For both fluence cases, the electron number density increases from an initial value of 10^{13} cm^{-3} to the order of 10^{21} cm^{-3} in less than one picosecond after the arrival of the peak intensity. This density is characteristic of the onset of material breakdown in semiconductors, indicating the potential onset of ablation for both cases [31,34]. The generation of free-carrier electrons causes the electron-system temperature to rise to 2.9×10^4 K for a fluence of 0.37 J/cm^2 and to 1.6×10^4 K for a fluence of 0.22 J/cm^2. The earlier plateau in carrier temperature is due to competing mechanisms, such as heat capacity of carriers and the temporal gradient of carrier density [35]. The higher electron temperature allows stronger coupling of thermal energy to the material lattice, causing the lattice temperature to rise to nearly 2100 K for the higher fluence, and ~1400 K for the lower fluence. Both predicted surface temperatures exceed the Ge melting temperature of 1213 K [33]. The TTM does not simulate phase change, so for the lower fluence case, only the onset of melting, confined to nanometer-order depth, is predicted based on the amount of energy supplied to the simulated lattice voxel in comparison to the enthalpy of fusion for Ge (refer to Appendix).

Optical Materials EXPRESS

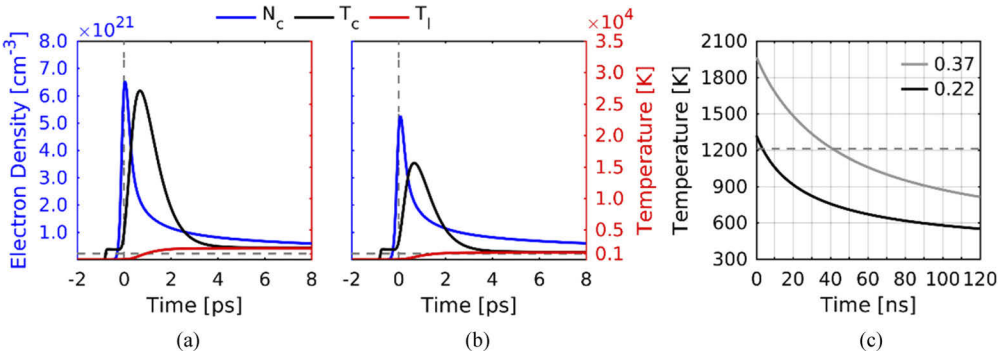

Fig. 1. TTM-simulated number density of free-carrier electrons (N_c), carrier-system temperature (T_c), and lattice temperature (T_l) at the location of peak intensity for incident-pulse fluences of (a) 0.37 J/cm^2 and (b) 0.22 J/cm^2. Times are relative to the arrival of the peak pulse intensity at 0 ps. (c) Dissipation of surface temperature following laser irradiation and electron/lattice temperature equilibration. In all plots, the dashed horizontal line corresponds to the Ge melting point at 1213 K [33].

Figure 1(c) compares heat diffusion behavior on the nanosecond timescale post electron/lattice temperature equilibration. The surface temperature induced by the 0.22 J/cm^2 fluence is predicted to dissipate to below the melting point an order of magnitude faster than for 0.37 J/cm^2 (4 ns vs. 40 ns). This indicates that reducing laser fluence can minimize the time over which detrimental thermal melting may occur [18]. Therefore, a fluence near 0.22 J/cm^2 is expected to induce ablation while controlling the extent of thermal effects.

2.2. *Impact of laser repetition rate and scanning speed*

To minimize the extent of heat accumulation, sufficient time must be allotted for heat diffusion to ensure that the surface can return near to its initial temperature prior to the next pulse incidence. The selected scan speed and repetition rate must control the temporal and spatial deposition of laser pulses to accommodate the material heat capacity and thermal conductivity [28].

The repetition rate and scan speed of our in-house femtosecond laser processing system can be nearly continuously tuned up to 2 MHz and 4 m/s. To avoid unbounded iterative numerical investigations, our previous numerical study of the impact of femtosecond laser parameters in semiconductor processing was consulted to identify operational ranges of scan speed and repetition rate to control heat accumulation [28]. A laser repetition rate on the order of 100 - 500 kHz and a scan speed on the order of 1 - 4 m/s demonstrated the capability to minimize heat accumulation, achieve uniform processing conditions, and control the onset of thermal effects during femtosecond laser processing [28].

A 250 kHz repetition rate and a 1 m/s scan speed were initially selected for line-configuration processing. This set of laser parameters adheres to the numerically-determined parameter ranges for low thermal impact processing in [28]. It also enables a pulse overlap of 93% of the 1/e^2 focal-spot diameter (~60 μm), which is within the reported range for smooth processing [22,24].

The TTM was used to evaluate and control heat accumulation and the onset of thermal effects during polishing, using a fluence of 0.22 J/cm^2, a scanning speed of 1 m/s, and a repetition rate of 250 kHz. Figure 2(a) shows that for each laser pulse, the surface temperature rises and then dissipates due to heat diffusion in the time between laser pulses. As more pulses are deposited, heat continues to accumulate until the thermal energy deposited by each laser pulse and the amount of heat dissipated between pulses reach equilibrium, controlled by the Ge thermal properties (specific heat capacity, thermal conductivity) [28]. Figure 2(b) shows that the base

Optical Materials EXPRESS

temperature achieved immediately prior to the next laser pulse begins to settle after 25 pulses at a temperature of just 345 K. Between 25 and 125 pulses, the base temperature is predicted to rise by only ten Kelvin to a value of 355 K. This demonstrates the capability for the selected laser parameters to produce controlled thermal processing conditions with minimal heat accumulation while producing a pulse overlap in the regime for uniform processing. Therefore, we find the combination of a 0.22 J/cm^2 laser fluence, a 250 kHz repetition rate, and a 1 m/s scan speed as a set of potential parameters for polishing.

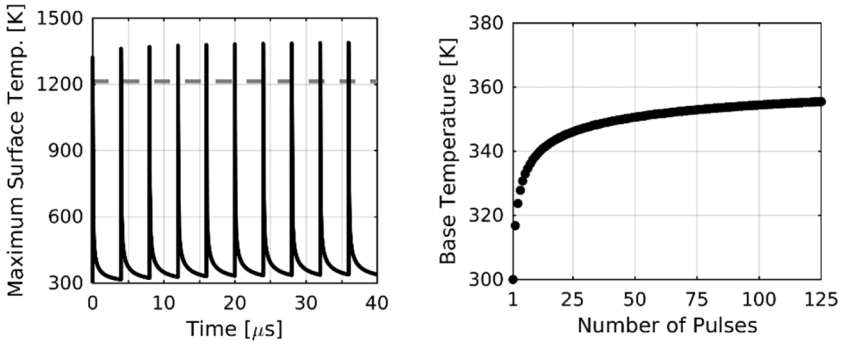

Fig. 2. Predicted surface temperature evolution due to femtosecond laser interaction using the initially determined set of laser parameters. (a) The maximum surface temperature corresponds to the location of peak fluence of the immediate-past pulse. (b) Predicted base surface temperature achieved prior to the next laser pulse for processing with 125 laser pulses.

3. Laser polishing experiments and results

3.1. Experimental validation of laser polishing parameters

Point and line processing experiments were carried out to evaluate the TTM-predicted laser parameters for femtosecond laser polishing of Ge. Experiments were performed on Ge substrates with <111> crystal orientation and ~1-nm root mean square (RMS) surface roughness, cleaned with isopropanol and/or methanol before irradiation. Substrates were processed using a 300 fs, 1030 nm Ytterbium fiber laser (Satsuma HP3, Amplitude Systémes). Beam attenuation, scanning, and focusing were controlled using integrated beam control and scanning hardware (LS-Shape and LS-Scan, Lasea). The 1/e^2 radius of the laser focal spot is 30 µm.

An experimental sensitivity study of laser fluence on ablation was carried out using single-shot laser pulses. Figure 3(a) shows the impact of laser fluence on the resulting area of ablation craters as measured by a Zygo NewView interferometric microscope. The relationship between the crater area A, and the laser fluence F_l, is defined as $A = (\pi \cdot w_o^2/2) \cdot \ln(F_l/F_{th})$, where F_{th} is the ablation threshold fluence and w_o is the 1/e^2 radius of the laser beam [30,36]. Fitting this relationship to the experimental data yielded an ablation threshold of approximately 0.2 J/cm^2 for Ge.

Figure 3(b) shows that a fluence of 0.22 J/cm^2, near the ablation threshold, is able to modify the surface region without generating rough central features like melt-induced ripples or nucleated gas bubbles [29]. This confirms the TTM-prediction that the 0.22 J/cm^2 fluence is capable of ablation-based material removal.

Line-configuration processing was also carried out to examine the combined effectiveness of the TTM-investigated fluence, repetition rate, and scan speed towards polishing Ge. Figure 4(a) shows that the parameters generate a uniformly colored processing track with potential surface smoothing, evidenced by "blurring" of the scratches which passed through the processing track.

Optical Materials EXPRESS

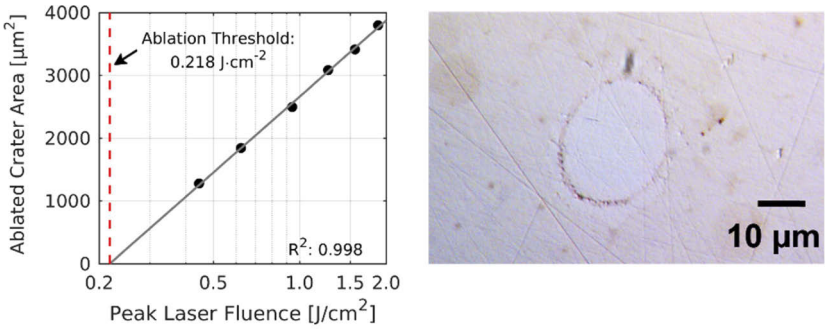

(a) (b)

Fig. 3. (a) Sensitivity of ablated crater area to single-shot laser fluence. (b) Optical microscope image of single-shot processing at a fluence of 0.22 J/cm^2.

Figure 4(b) shows that using a higher fluence of 0.37 J/cm^2 for the same repetition rate and scan speed produces rough structures in the center of the processed track. The structures have periodicity on the order of the laser wavelength resulting from interference between the incident electric field and the dense ionic plasma generated by the laser pulses [37]. They are also potentially exacerbated by the thermal impact of processing at higher fluences, indicated by the model-predicted lattice temperature of 2100 K (significantly above the Ge melting point of 1213 K) for processing with a fluence of 0.37 J/cm^2.

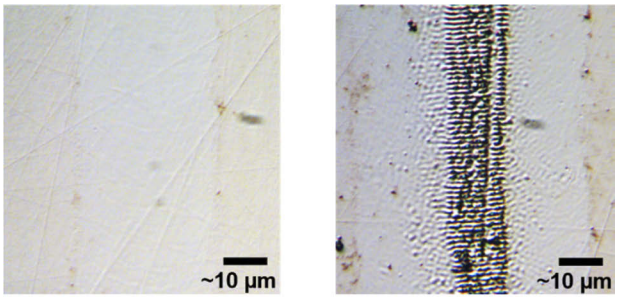

(a) (b)

Fig. 4. Optical micrographs of line processing using a 1 m/s scan speed and a 250 kHz repetition rate for two laser fluences: (a) 0.22 J/cm^2, (b) 0.37 J/cm^2. The processed region corresponds to the ~30-50 μm wide bright track and the structures therein.

According to the modeling results shown in Fig. 1(b) and (c) and the experimentally determined Ge ablation threshold, we determine that ablation and the onset of melting will most likely occur simultaneously during laser polishing of Ge. We therefore aim to achieve as close to a nonthermal ablation state as possible to minimize thermal effects and heat-affected zones. The experimental results for point and line processing guided by the TTM model prediction confirm that selecting a laser fluence near the ablation threshold and a repetition rate and scanning speed to minimize heat accumulation is a strategy towards achieving smooth femtosecond laser polishing.

3.2. Demonstration of laser polishing on Ge

Femtosecond laser polishing experiments were carried out using the experimentally validated set of laser parameters for smooth processing in Fig. 4(a). A strategy to generate overlapping lines of processing was devised to polish a region of the Ge surface (~0.5 mm × 0.5 mm). Lines were

Optical Materials EXPRESS

marked unidirectionally with line overlap initially set to 75% of the laser focal spot diameter to maintain processing efficiency [22]. A completed scan over the defined polishing area is referred to as a "polishing pass".

Figure 5 compares an unprocessed (control) Ge surface and a laser-polished Ge surface generated using 20 polishing passes. The representative optical micrographs in Fig. 5(a) and (b) show that the control surface contains defects including scratches and discoloration which are not evident in the laser-polished surface.

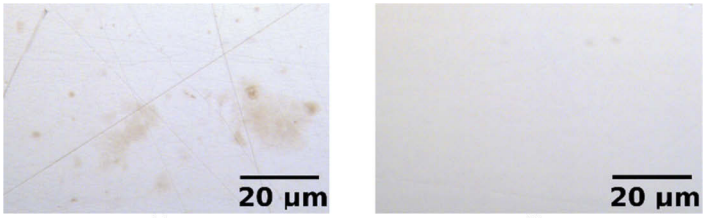

(a) (b)

Fig. 5. Comparison of optical micrographs within (a) unprocessed and (b) 20-pass laser-polished surface regions.

Figure 6(a) shows a surface height map of a 20-pass laser-polished area and the surrounding unprocessed surface (measured using a Zygo NewView). The depth of material removal in the polished area is 6 nm. The slight deepening of the removal at the top and bottom edges of the polished region follows from increased laser dwell time due to scanning acceleration and the slight striation in the area follows from the initial line overlap selection, both of which are undergoing correction. The average RMS roughness in the center of the laser-polished area is 0.826 ± 0.102 nm, and that of the surrounding unprocessed area is 0.824 ± 0.185 nm (averages calculated over five, 150 µm × 150 µm regions). Representative zoomed-in surface profiles of unprocessed and laser-polished areas are shown in Fig. 6(b) and 6(c), corresponding to the locations of the images in Fig. 5. The femtosecond-laser-polished area maintained single-digit nanometer surface roughness quality, e.g., 0.72 nm RMS in comparison to 0.78 nm in the unprocessed region.

The results in Fig. 5 and Fig. 6 demonstrate that the devised laser polishing strategy is able to effectively remove surface defects while maintaining sub-nanometer optic-quality surface roughness, revealing the capability of femtosecond laser polishing for high-precision material removal tasks.

The controllability of material removal by femtosecond laser polishing was investigated by varying the number of polishing passes and/or the overlap of the scanned lines. Figure 7(a) shows that the material removal depth increases from 4 nm to approximately 30 nm when increasing the number of polishing passes from 15 to 100. The optic-quality surface with $\lesssim$1.5 nm RMS roughness is consistently maintained for various material removal depths. Figure 7(b) shows that material removal depth linearly follows the total deposited laser energy resulting from various combinations of line overlaps and numbers of polishing passes. This demonstrates that total deposited energy can be used as a metric by which laser parameter combinations can be determined to maximize the processing efficiency, accommodate larger-scale polishing tasks and rougher surfaces, and achieve dynamic control of material removal for extension to complex freeform surface geometries. The material removal rate for the femtosecond laser polishing experiments in Fig. 7 is on the order of 10^{-4} mm^3/min, comparable to certain ion-beam figuring processes with small beam sizes, used in final finishing of freeform optics [38,39]. Using the metric of total deposited energy, laser-based material removal rate can be improved via determining an optimal combination of focal spot size, line overlap, scanning speed, and repetition rate, further competing with ultraprecision final-finishing techniques like magnetorheological finishing.

Optical Materials EXPRESS

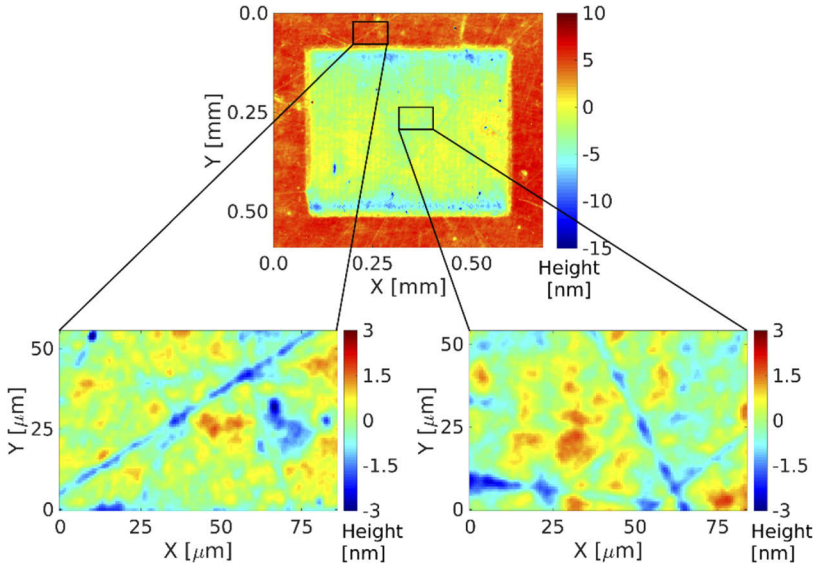

Fig. 6. Full-area height map of Ge polishing using 20 laser passes (central rectangular feature) and zoomed-in surface profiles for unprocessed and polished surface regions.

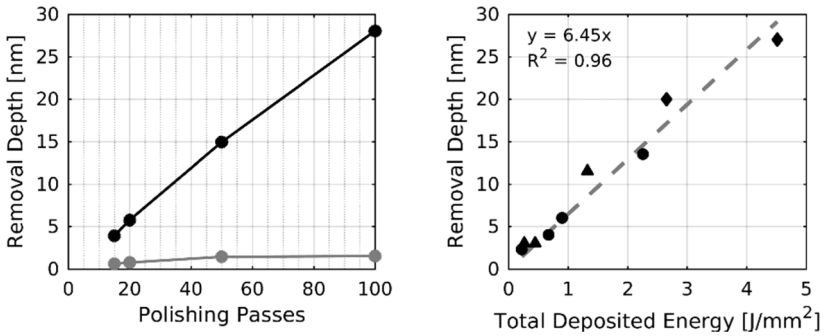

(a) (b)

Fig. 7. (a) Impact of the number of polishing passes on material removal depth (black) and the resulting RMS surface roughness (gray). (b) Material removal depth versus total deposited energy varied by polishing with: (▲) 10 passes/scan-line overlap of ~60 to 90% of the laser spot diameter, (♦) 100 passes/scan-line overlap of ~60 to 75%, and (●) 5 to 20 passes/75% scan-line overlap.

4. Discussion on the polishing mechanism

The physical mechanism for achieving smooth polishing is attributed to high-precision laser ablation with controlled thermal impact. Ablation is predicted because the 0.22 J/cm^2 laser fluence is at the experimentally-determined ablation threshold for Ge (Fig. 3(a)) and the TTM-predicted number density rises to 10^{21} cm^{-3} (Fig. 1), characteristic of the onset of material breakdown in semiconductor materials [31,40]. Controllable ablation at this low fluence is experimentally demonstrated in Fig. 7(a): near-linear increase in removal depth with increasing number of polishing passes while maintaining $\lesssim$1.5 nm RMS roughness. We expect that the onset of melting may also contribute to the smoothing mechanism since the TTM predicts that the 0.22 J/cm^2 fluence drives the surface temperature to slightly exceed the Ge melting point.

Optical Materials EXPRESS

However, only the onset of thermal melting, controlled to the nanometer order, is expected due to the small magnitude of the temperature rise/short time spent above the melting point (refer to Appendix). Minimal/controlled melting is experimentally supported as no melt-ejection, e.g., no "splashed" material or material pileup, is evident along the ablated track, as demonstrated in other high-thermal-impact processing experiments [28]. This high-precision melt-depth is a significant improvement over continuous-wave and micro/nanosecond-pulsed laser polishing strategies which generate melt/heat-affected zones with depths up to tens of micrometers [16].

Other laser-induced-breakdown phenomena could also play a role in laser polishing. For example, nonthermal melting and/or laser annealing can cause lattice ordering/disordering in single-crystal semiconductors [18,41,42], potentially contributing to smoothing the Ge surface. These phenomena can occur once approximately ten percent of the valence band electrons have been promoted to the conduction band, signified by electron densities in the range of 10^{21} - 10^{22} cm^{-3} [31,40,41,43], consistent with the TTM-predicted electron densities in Section 2. However, the TTM cannot independently assess or differentiate these phenomena from ablation-based material removal.

5. Conclusion

Femtosecond-laser-based polishing was investigated to address the need for high-precision, high-flexibility techniques for forming and finishing freeform optical surfaces. A strategy for polishing of Ge, combining modeling, experimental methods, and demonstrations, was established to precisely remove material while maintaining optical surface quality. A TTM of scanning femtosecond laser processing was built to investigate the combined impact of laser parameters on Ge ablation and surface temperature. Using the model, we successfully determined a set of laser polishing parameters which produce controlled ablation and minimized thermal effects on the Ge surface, validated by experiments. The TTM acts as a predictive tool/step in the polishing process to understand and determine laser parameter combinations to best approach nonthermal ablation for the polishing application. It further eliminates the need for time/waste-expensive iterative parameter-determination experiments. For the first time, to our knowledge, we demonstrated model-guided femtosecond-laser-based polishing of Ge with tunable material removal and maintained the optic-quality surface with roughness of ~1 nm. We also established a metric to scale-up the material removal towards larger polishing tasks and non-flat surfaces. The controllable material removal with high-spatial precision, geometrical flexibility, and optic-quality surface roughness establish the foundation for optics polishing/fabrication using femtosecond lasers and position the technique for advanced optical fabrication applications including freeform optics.

Appendix

Two-temperature model formulation

The TTM of scanning, multi-pulse femtosecond laser-material interaction presented in Section 2 was based on a model originally formulated to simulate femtosecond laser processing of silicon [30]. Adapting the model for Ge required identification and integration of material properties to effectively account for its electronic and thermal behaviors and re-derivation of certain equations to accommodate these changes; the original numerical algorithm was maintained. Therefore, this Appendix only describes relevant TTM modifications to simulate Ge. We direct the reader to our separate publication for information on the numeric algorithm devised to implement the TTM in three dimensions [30].

The TTM simulates the following phenomena for each incident laser pulse: (1) absorption of laser pulse energy, (2) generation of free-carrier electrons, (3) temperature of the electron

Optical Materials EXPRESS

system, and (4) temperature of the material lattice. These phenomena are respectively described by Eqs. (1)–(4). The TTM equations are established under the relaxation-time approximation of the Boltzmann equation and assumptions outlined in references [31,32]. To enable numerical implementation in C++, equations were solved by hand using a numerical finite difference scheme. The key parameters and coefficients for all equations are detailed in Table 1.

Table 1. Key parameters for the Ge TTM

Parameter	Symbol	Value	Unit	Ref.
Photon energy ($\lambda = 1030$ nm)	E_{photon}	1.2	eV	—
Bandgap Energy	E_{gap}	$0.803 - 3.9 \times 10^{-4} \cdot T_l$	eV	[31]
Linear absorption coefficient	α	$1.4\times10^{4} \cdot (1 + T_l / 2000)$	cm^{-1}	[44]
Free-carrier absorption cross-section	Θ	6.6×10^{-20}	cm^2	[45,47]
Auger recombination coefficient	γ	2×10^{-31}	cm^6/s	[31,44]
Ambipolar diffusion coefficient†	D	$65 \cdot (T_l/ 300)^{-1.5}$	cm^2/s	[31,44]
Electron relaxation time	τ	$400 \cdot \left(1 + \left(\frac{N_c}{2 \times 10^{21}}\right)^2\right)$	fs	[35]
Electronic heat capacity	C_{e-h}	$3N_c k_b$	$J/(cm^3 \cdot K)$	[31]
Lattice heat capacity	C_l	$1.7 \cdot (1 + T_l/6000)$	$J/(cm^3 \cdot K)$	[31,44]
Lattice thermal conductivity	κ_l	$675 \cdot {T_l}^{-1.23}$	W/(cm·K)	[31]

†Related to $\bar{J}, \bar{W}$

When a laser pulse is incident on a material, a fraction of the energy is reflected away ($R = 0.39$ for NIR light on Ge [44]) and the remainder of the energy is absorbed by the bulk.

$$dI/dz = -(\alpha + \Theta N_c)I \tag{1}$$

Equation 1 describes the fall-off of intensity along the direction of laser propagation due to energy absorption. When irradiating Ge with 1030 nm light, linear absorption (α) dominates since the photon energy is much higher than the material bandgap ($E_{photon} = 1.2$ eV; $E_{gap} \approx 0.8$ eV). Energy absorption drives the number density of generated free-carrier electrons, N_c, orders of magnitude above its initial, intrinsic value of 10^{13} cm^{-3}, so free-carrier absorption (ΘN_c) also plays a role. The impact of two-photon absorption is negligible when $E_{photon} >> E_{gap}$, therefore, it is not considered in this model.

$$\frac{\partial N_c}{\partial t} = \frac{\alpha I}{E_{photon}} - \gamma {N_c}^3 - \nabla \cdot \bar{J} \tag{2}$$

Equation (2) shows that the number density of free-carrier electrons is increased by energy absorption and respectively affected by Auger recombination and ambipolar diffusion [30]. Ambipolar diffusion holds under the condition that the carriers follow a Maxwell-Boltzmann distribution [32]. Impact ionization is not considered because it is negligible in comparison to the dominant effect of linear absorption [44]. The onset of material breakdown, e.g., ablation and nonthermal melting, can occur once the number density of free-carrier electrons reaches a critical density on the order of 10^{21}–10^{22} cm^{-3} [31,40,41,43,45]. However, the model does not simulate changes in the electronic or lattice structure for densities in this range, as the exact critical density for breakdown on Ge via 1030 nm radiation is not well-established. Therefore, this density range acts only as an indicator of potential breakdown.

$$C_{e-h}\frac{\partial T_c}{\partial t} = (\alpha + \Theta N_c)I - \left[\frac{C_{e-h}}{\tau}(T_c - T_l) + \nabla \cdot \bar{W} + \frac{\partial N_c}{\partial t} \cdot (E_{gap} + 3k_b T_c) + \frac{\partial E_{gap}}{\partial t} \cdot N_c\right] \tag{3}$$

Equation 3 describes the corresponding temperature of the carrier system, increased by energy absorption and decreased by coupling of thermal energy from the carriers (T_c) to the lattice

Optical Materials EXPRESS

(T_l) according to the electronic heat capacity (C_{e-h}) and relaxation time (τ), ambipolar energy current ($\bar{W}$), and respective changes in kinetic and bandgap energies (where, k_b is the Boltzmann constant).

$$C_l \frac{\partial T_l}{\partial t} = \frac{C_{e-h}}{\tau}(T_c - T_l) + \nabla \cdot (\kappa_l \nabla T_l) \tag{4}$$

Equation (4) describes the evolution of the lattice temperature throughout the laser-material interaction process. Thermal energy from the carrier system is coupled to the lattice until the systems reach thermal equilibrium. Upon temperature equilibration, Eq. (4) becomes the classical heat conduction equation which describes bulk heat diffusion according to the material heat capacity (C_l) and thermal conductivity (κ_l) in the time between laser pulses [30,46].

Influence parameters

An exploration of the influence of the free-carrier absorption cross section and electron relaxation time on the simulation results was conducted to address the wide range of values reported in the literature [25,32,35,48]. For each of the investigated influence parameter values, the behavior of the TTM-predicted electron number density, electron temperature, and lattice temperature were compared to the results of molecular dynamics (MD) simulations of femtosecond laser/Ge interaction [35]. The free-carrier absorption cross section and electron relaxation time in Table 1 were selected for the model because they enable the number density and temperatures to rise and fall to similar orders of magnitude on consistent timescales with the MD simulations.

Prediction of thermal melting

Although the TTM can predict the surface temperature rise in the material lattice, it does not simulate solid/liquid phase change. Therefore, the surface temperature prediction is treated only as an indication of thermal energy transfer to the lattice. In order for the laser to thermally melt the material surface, enough energy must be supplied after the melting point has been reached to overcome the enthalpy of fusion required for solid-liquid phase change (36.94 kJ/mol for Ge [33]). In a TTM lattice voxel with dimensions of 2 µm x 2 µm x 5 nm, this would correspond to an energy of ~50 pJ, calculated as $\Delta E = (T_{TTM} - T_{melt}) \cdot c_v V$, where T_{TTM} is the TTM-predicted lattice temperature, V is the voxel volume, T_{melt} is the Ge melting temperature, and c_v is the volumetric specific heat capacity [28]. For the 0.22 J/cm^2 simulation in Section 2, the energy supplied to the surface voxel after the melting point is reached is just 9 pJ, less than 20% of the energy required for full melting. Hence, we predict only the onset of thermal melting at the surface, and that the melt depth is constrained to the single-digit nanometer order.

Funding

National Science Foundation (NSF) I/UCRC Center for Freeform Optics (IIP-1338877, IIP-1338898, IIP-1822026, IIP-1822049); Fuzehub (Jeff Lawrence Innovation Fund).

Acknowledgement

We thank François Piché, Edward Fess, and Steve VanKerkhove (Corning, Fairport NY) for assistance obtaining height maps of the laser-polished samples and Dr. Surendra Gupta (Rochester Institute of Technology) for assistance with optical microscopy. We are also thankful for insightful exchanges on Two-Temperature Modeling with Dr. Henry van Driel, Dr. Edwin Hach, Ryan Scott, and Joshua Frechem.

References

1. A. Bauer and J. P. Rolland, "Visual space assessment of two all-reflective, freeform, optical see-through head-worn displays," Opt. Express **22**(11), 13155–13163 (2014).
2. G. W. Forbes, "Characterizing the shape of freeform optics," Opt. Express **20**(3), 2483–2499 (2012).

Optical Materials EXPRESS

3. F. Z. Fang, X. D. Zhang, A. Weckenmann, G. X. Zhang, and C. Evans, "Manufacturing and measurement of freeform optics," CIRP Ann. **62**(2), 823–846 (2013).
4. C. Miao, J. C. Lambropoulos, and S. D. Jacobs, "Process parameter effects on material removal in magnetorheological finishing of borosilicate glass," Appl. Opt. **49**(10), 1951–1963 (2010).
5. D. Li, B. Wang, Z. Qiao, and X. Jiang, "Ultraprecision machining of microlens arrays with integrated on-machine surface metrology," Opt. Express **27**(1), 212–224 (2019).
6. Z. Zhu, X. Zhou, D. Luo, and Q. Liu, "Development of pseudo-random diamond turning method for fabricating freeform optics with scattering homogenization," Opt. Express **21**(23), 28469–28482 (2013).
7. D. Li, N. Li, X. Su, K. Liu, P. Ji, and B. Wang, "Modelling of removal characteristics and surface morphology formation in capacitively coupled atmospheric pressure plasma processing of fused silica optics," Opt. Mater. Express **9**(4), 1893–1906 (2019).
8. X. Su, P. Ji, K. Liu, D. Walker, G. Yu, H. Li, D. Li, and B. Wang, "Combined processing chain for freeform optics based on atmospheric pressure plasma processing and bonnet polishing," Opt. Express **27**(13), 17979–17992 (2019).
9. T. Arnold, G. Böhm, R. Fechner, J. Meister, A. Nickel, F. Frost, T. Hänsel, and A. Schindler, "Ultra-precision surface finishing by ion beam and plasma jet techniques—status and outlook," Nucl. Instrum. Methods Phys. Res., Sect. A **616**(2-3), 147–156 (2010).
10. H. Shahinian, M. Hassan, H. Cherukuri, and B. A. Mullany, "Fiber-based tools: material removal and mid-spatial frequency error reduction," Appl. Opt. **56**(29), 8266–8274 (2017).
11. J. D. Owen, J. A. Shultz, T. J. Suleski, and M. A. Davies, "Error correction methodology for ultra-precision three-axis milling of freeform optics," CIRP Ann. **66**(1), 97–100 (2017).
12. M. J. Matthews, S. T. Yang, N. Shen, S. Elhadj, R. N. Raman, G. Guss, I. L. Bass, M. C. Nostrand, and P. J. Wegner, "Micro-shaping, polishing, and damage repair of fused silica surfaces using focused infrared laser beams," Adv. Eng. Mater. **17**(3), 247–252 (2015).
13. S. Heidrich, A. Richmann, P. Schmitz, E. Willenborg, K. Wissenbach, P. Loosen, and R. Poprawe, "Optics manufacturing by laser radiation," Opt. Lasers Eng. **59**, 34–40 (2014).
14. T. L. Perry, D. Werschmoeller, X. Li, F. E. Pfefferkorn, and N. A. Duffie, "The effect of laser pulse duration and feed rate on pulsed laser polishing of microfabricated nickel samples," J. Manuf. Sci. Eng. **131**(3), 031002 (2009).
15. E. V. Bordatchev, A. M. K. Hafiz, and O. R. Tutunea-Fatan, "Performance of laser polishing in finishing of metallic surfaces," Int. J. Adv. Manuf. Technol. **73**(1-4), 35–52 (2014).
16. M. Vadali, C. Ma, N. A. Duffie, X. Li, and F. E. Pfefferkorn, "Effects of pulse duration on laser micro polishing," J. Micro Nano-Manuf. **1**(1), 011006 (2013).
17. J. D. Morrow, J. Vockrodt, K. Klingbeil, and F. E. Pfefferkorn, "Predicting laser polishing outcomes at edge features," J. Laser Appl. **29**(1), 011703 (2017).
18. S. K. Sundaram and E. Mazur, "Inducing and probing non-thermal transitions in semiconductors using femtosecond laser pulses," Nat. Mater. **1**(4), 217–224 (2002).
19. S. M. Eaton, M. L. Ng, R. Osellame, and P. R. Herman, "High refractive index contrast in fused silica waveguides by tightly focused, high-repetition rate femtosecond laser," J. Non-Cryst. Solids **357**(11-13), 2387–2391 (2011).
20. R. M. Carter, J. Chen, J. D. Shephard, R. R. Thomson, and D. P. Hand, "Picosecond laser welding of similar and dissimilar materials," Appl. Opt. **53**(19), 4233–4238 (2014).
21. Z. Deng, Q. Yang, F. Chen, X. Meng, H. Bian, J. Yong, C. Shan, and X. Hou, "Fabrication of large-area concave microlens array on silicon by femtosecond laser micromachining," Opt. Lett. **40**(9), 1928–1931 (2015).
22. B. Neuenschwander, B. Jaeggi, M. Zimmermannn, V. Markovic, B. Resan, K. Weingarten, R. de Loor, and L. Penning, "Laser surface structuring with 100 W of average power and sub-ps pulses," J. Laser Appl. **28**(2), 022506 (2016).
23. J. Bliedtner, C. Schindler, M. Seiler, S. Wächter, M. Friedrich, and J. Giesecke, "Ultrashort pulse laser material processing," Laser Tech. J. **13**(5), 46–50 (2016).
24. A. M. K. Hafiz, E. V. Bordatchev, and R. O. Tutunea-Fatan, "Experimental analysis of applicability of a picosecond laser for micro-polishing of micromilled Inconel 718 superalloy," Int. J. Adv. Manuf. Technol. **70**(9-12), 1963–1978 (2014).
25. Y. D. Chen, W. J. Tsai, S. H. Liu, and J. B. Horng, "Picosecond laser pulse polishing of ASP23 steel," Opt. Laser Technol. **107**, 180–185 (2018).
26. B. N. Chichkov, C. Momma, S. Nolte, F. von Alvensleben, and A. Tünnermann, "Femtosecond, picosecond and nanosecond laser ablation of solids," Appl. Phys. A **63**(2), 109–115 (1996).
27. B. Neuenschwander, B. Jaeggi, and M. Schmid, "From fs to sub-ns: dependence of the material removal rate on the pulse duration for metals," Phys. Procedia **41**, 794–801 (2013).
28. L. L. Taylor, J. Qiao, and J. Qiao, "Optimization of femtosecond laser processing of silicon via numerical modeling," Opt. Mater. Express **6**(9), 2745–2758 (2016).
29. J. Bonse, S. Baudach, J. Krüger, W. Kautek, and M. Lenzner, "Femtosecond laser ablation of silicon-modification thresholds and morphology," Appl. Phys. A: Mater. Sci. Process. **74**(1), 19–25 (2002).
30. L. L. Taylor, R. E. Scott, and J. Qiao, "Integrating two-temperature and classical heat accumulation models to predict femtosecond laser processing of silicon," Opt. Mater. Express **8**(3), 648–658 (2018).
31. J. K. Chen, D. Y. Tzou, and J. E. Beraun, "Numerical investigation of ultrashort laser damage in semiconductors," Int. J. Heat Mass Transfer **48**(3-4), 501–509 (2005).

Optical Materials EXPRESS

32. H. M. Van Driel, "Kinetics of high-density plasmas generated in Si by 1.06- and 0.53-um picosecond laser pulses," Phys. Rev. B **35**(15), 8166–8176 (1987).
33. J. R. Rumble, D. R. Lide, and T. J. Bruno, *CRC Handbook of Chemistry and Physics: A Ready-Reference Book of Chemical and Physical Data* (CRC Press, 2018).
34. J. Bonse, G. Bachelier, J. Siegel, and J. Solis, "Time- and space-resolved dynamics of melting, ablation, and solidification phenomena induced by femtosecond laser pulses in germanium," Phys. Rev. B **74**(13), 134106 (2006).
35. Y. Gan and J. K. Chen, "Numerical analysis of ultrashort pulse laser-induced thermomechanical response of germanium thin films," Nanoscale Microscale Thermophys. Eng. **16**(4), 274–287 (2012).
36. J. M. Liu, "Simple technique for measurements of pulsed gaussian-beam spot sizes," Opt. Lett. **7**(5), 196–198 (1982).
37. D. R. Austin, K. R. P. Kafka, Y. H. Lai, Z. Wang, K. Zhang, H. Li, C. I. Blaga, A. Y. Yi, L. F. DiMauro, and E. A. Chowdhury, "High spatial frequency laser induced periodic surface structure formation in germanium under strong mid-IR fields," J. Appl. Phys. **120**(14), 143103 (2016).
38. J. Bauer, A. Lehmann, M. Ulitschka, Y. Li, and T. Arnold, "Finishing of metal optics by ion beam technologies," Opt. Eng. **58**(9), 1–12 (2019).
39. I. F. Stowers, R. Komanduri, and E. D. Baird, "Review of precision surface generating processes and their potential application to the fabrication of large optical components," Proc. SPIE **0966**, 62 (1989).
40. P. Stampfli and K. H. Bennemann, "Theory for the instability of the diamond structure of Si, Ge and C induced by a dense electron-hole plasma," Phys. Rev. B **42**(11), 7163–7173 (1990).
41. K. Sokolowski-Tinten, J. Bialkowski, M. Boing, A. Cavalleri, and D. von der Linde, "Thermal and nonthermal melting of gallium arsenide after femtosecond laser excitation," Phys. Rev. B **58**(18), R11805 (1998).
42. J. A. Van Vechten, R. Tsu, and F. W. Saris, "Nonthermal pulsed laser annealing of Si; plasma annealing," Phys. Lett. A **74**(6), 422–426 (1979).
43. A. Rousse, C. Rischel, S. Fourmaux, I. Uschmann, S. Sebban, G. Grillon, Ph. Balcou, E. Forster, J. P. Geindre, P. Audebert, J. C. Gauthier, and D. Hulin, "Non-thermal melting in semiconductors measured at femtosecond resolution," Nature **410**(6824), 65–68 (2001).
44. M. I. Gallant and H. M. van Driel, "Infrared reflectivity probing of thermal and spatial properties of laser-generated carriers in germanium," Phys. Rev. B **26**(4), 2133–2146 (1982).
45. J. Thorstensen and S. E. Foss, "Temperature dependent ablation threshold in silicon using ultrashort laser pulses," J. Appl. Phys. **112**(10), 103514 (2012).
46. H. S. Carslaw and J. C. Jaeger, *Conduction of Heat in Solids* (Clarendon Press, 1959).
47. S. C. Baker-Finch, K. R. McIntosh, D. Yan, K. C. Fong, and T. C. Kho, "Near-infrared free carrier absorption in heavily doped silicon," J. Appl. Phys. **116**(6), 063106 (2014).
48. D. Agassi, "Phenomenological model for pisosecond-pulse laser annealing of semiconductors," J. Appl. Phys. **55**(12), 4376–4383 (1984).